Project Report
TIP-121

Computational Modeling of Additive Manufacturing by Power Bed Laser Fusion: FY19 Engineering Research Technical Investment Program

E.M. Parsons

14 May 2020

Lincoln Laboratory
MASSACHUSETTS INSTITUTE OF TECHNOLOGY
LEXINGTON, MASSACHUSETTS

This material is based upon work supported by the United States Air Force under Air Force Contract No. FA8702-15-D-0001.

This report is the result of studies performed at Lincoln Laboratory, a federally funded research and development center operated by Massachusetts Institute of Technology. This material is based upon work supported under Air Force Contract No. FA8702-15-D-0001. Any opinions, findings, conclusions or recommendations expressed in this material are those of the author(s) and do not necessarily reflect the views of the U.S. Air Force.

DESTRUCTION NOTICE

For unclassified, limited distribution documents, destroy by any method that will prevent disclosure of the contents or reconstruction of the document.

Massachusetts Institute of Technology
Lincoln Laboratory

Computational Modeling of Additive Manufacturing by Power Bed Laser Fusion: FY19 Engineering Research Technical Investment Program

E.M. Parsons
Group 74

Project Report TIP-121
14 May 2020

Lexington Massachusetts

This page intentionally left blank.

TABLE OF CONTENTS

This page intentionally left blank.

LIST OF FIGURES

LIST OF FIGURES
(Continued)

LIST OF FIGURES
(Continued)

This page intentionally left blank.

1. INTRODUCTION TO ADDITIVE MANUFACTURING BY SELECTIVE LASER MELTING

Additive manufacturing (AM) or "3D printing" has had a huge impact on numerous sectors at scales ranging from microfabrication to big area manufacturing (size of meters). Many predict that it will soon be recognized as the technology behind the third industrial revolution. It is defined by the ISO/ASTM as "the process of joining materials to make parts from 3D model data, usually layer upon layer, as opposed to subtractive and formative manufacturing methodologies." With additive manufacturing, parts of complex geometry can be built with a single machine operation and without any special masks, tooling, dies, or fixtures. Originally used primarily for fabrication of prototypes and models of design concepts, various AM methods are presently capable of producing functional devices, components, and structures constructed from numerous types of materials.

MIT LL is increasingly using the AM process selective laser melting (SLM) to build metal structural components for prototypes. The highest resolution form of metal printing, SLM is a powder bed fusion process in which selective areas of a bed of metal powder are fully melted and consolidated with a high-energy laser (Figure 1). Once fusion of a given layer is complete, the build platform is lowered, and another layer is spread or "recoated" over the platform. SLM is ideal for production of the low volumes of high-value parts that are typical of the defense and aerospace sectors. Heavily light-weighted parts and parts with internal channels or cavities can be manufactured, sometimes reducing to a single piece an assembly that would otherwise consist of dozens of separate components joined together. In many cases, SLM enables fabrication of parts with complex features that could not be produced at all with conventional methods.

Despite the great potential of SLM to improve performance and reduce lead times, SLM alloy properties, part quality, and process reliability must improve for SLM to become broadly used in critical structural applications. Two shortcomings prevent SLM from gaining widespread adoption. First, part quality and performance are functions of the part geometry and build orientation. Because the understanding of the relationships between process parameters, fused material properties and part performance is limited, process parameters developed for prismatic samples can result in defects, warping, uncertain material properties, and residual stresses. Second, processing by SLM is presently limited to just a handful of plain, unreinforced alloys that exhibit unremarkable mechanical properties. For example, the only aluminum alloys commonly used with SLM are AlSi10Mg and AlSi12, and no highly reinforced metal matrix composites are commercially available. AlSi10Mg and AlSi12 were designed specifically for casting and exhibit yield strength, ductility, and fatigue strength substantially inferior to the properties of frequently used wrought alloys or metal matrix composites. Development of new alloys or metal matrix composites for AM would entail numerous experimental trials, with process parameters selected by trial and error, requiring many years and costing tens of millions of dollars or more.

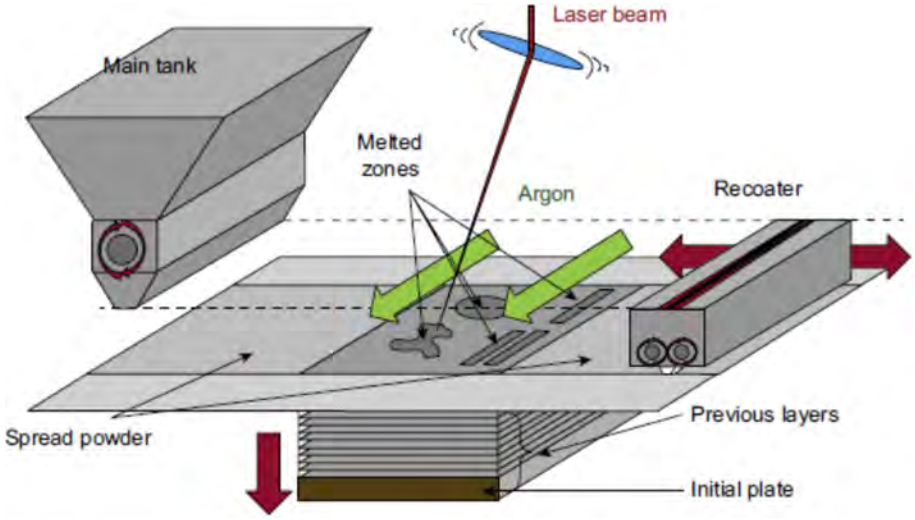

Figure 1. Schematic of the build chamber of a selective laser melting machine, showing the laser beam, build plate, powder recoater, and flow of inert gas. This example uses a hopper to deposit powder (top left), similar to the design of the micro-SLM.

2. MOTIVATION: THE NEED FOR MATHEMATICAL MODELS OF SLM

Laser consolidation by SLM is exceptionally complex because it involves multiple types of physics and numerous process parameters. The physics include phase changes, mass transfer, and several modes of heat transfer (Figure 2a). The process parameters include both laser parameters (beam diameter, velocity, and scan pattern) and powder bed parameters (layer thickness, packing density, absorptivity, conductivity, and initial temperature), as illustrated in Figure 2b. All these parameters combine to determine the consolidated material properties and part performance.

Because of the complexity of the SLM process, analytical models, scaling relations, and numerical models of the laser heating process have been developed for the purpose of planning experiments, interpreting experimental results, and optimizing process parameters. Specifically, the goal is to relate the machine and powder bed parameters to the melt pool characteristics and thermal history so that microstructure and part quality can be optimized.

In this program, we are developing physics-based modeling and simulation capabilities that will be used to optimize SLM process parameters and to design new materials for SLM. Predictive modeling is needed to relate the numerous process parameters to the local melt pool characteristics and thermal history that produce the desired microstructures, material properties, and part performance. By controlling melt pool temperature and aspect ratio, we can prevent defects due to lack of fusion (energy too low), keyholing, evaporation of alloying elements (energy too high), and balling of the melt pool (scan velocity too high). In addition, predictions of melt pool dimensions can be used to determine hatch spacing and powder layer thickness for new materials or new process parameters. At the level of microstructure, local thermal gradients, solidification velocities, and cooling rates can be manipulated to engineer grain type, size, and orientation. Finally, residual stresses that cause defects, warping, and poor part performance can be reduced by designing scan strategies that produce uniform heating and cooling.

In one application, these computational tools can be used to tune process parameters based on the geometry of the part. Process parameters determined experimentally are strictly only valid for the geometry of the test samples. In an actual part, thermal conditions and strains vary with location, potentially causing defects and the development of residual stresses that can reduce dimensional accuracy and lead to failure during the build or in the field. Optimal process parameters, specific to the geometry of the part being built, can only be systematically determined by physically motivated simulation of the melting and consolidation processes.

In the second application, the computational tools can be used to optimize material microstructure and properties, both for improving the processing of existing SLM alloys and for developing new alloys and metal matrix composites for SLM. Although the yield strength, fatigue strength, and toughness of existing SLM alloys are typically inferior to those of their wrought counterparts, the properties of alloys designed specifically for the thermal cycling and high cooling rates of SLM have the potential to match or exceed those of wrought alloys. Simulation will

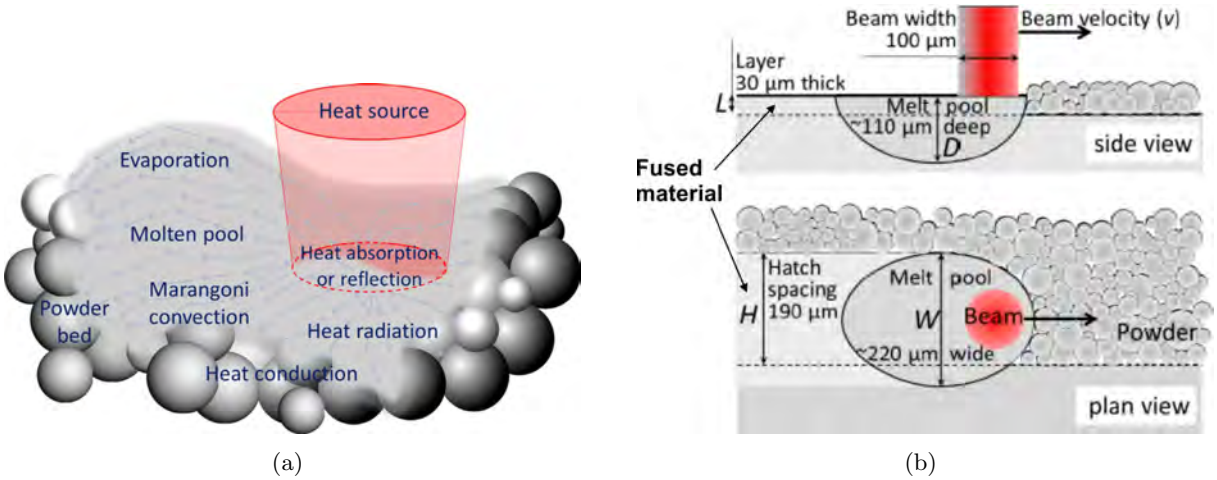

Figure 2. Schematics of laser heating and melt pool formation during SLM. (a) Multiple types of heat transfer occur simultaneously. (b) SLM process parameters include beam size, beam velocity, powder layer thickness, and hatch spacing.

provide detailed knowledge of the material's thermal history during SLM, including cooling rates, temperature gradients, and solidification velocities. These process conditions, together with the material's elemental composition, can then be designed to control the grain morphology and formation of phases, while also preventing loss of alloying elements and material defects such as the solidification cracking that frequently occurs in high-alloy metals. (For example, disrupting the formation of columnar grains and promoting the formation of equiaxed, fine-grained microstructures can enhance fatigue strength and prevent hot tearing during solidification.) Furthermore, modeling will be critical in the current effort at MIT LL to develop metal matrix composites for SLM. The modeling capabilities developed in this program will be used to predict how the ceramic content of the powder changes the melt pool characteristics. The effect of powder bed properties such as packing density, absorptivity, and effective thermal conductivity can be simulated as a function of ceramic content, facilitating navigation of the numerous trade-offs associated with SLM of multimaterial, multiphase powder beds. For example, on the one hand, the high absorptivity of the ceramic phase should reduce the laser power required (aluminum has very low absorptivity). However, on the other hand, an increase in melt pool temperature may be necessary to counteract the increase in viscosity caused by the ceramic particles, which can impede the wetting of the previously consolidated layer by the melt pool.

3. GOVERNING EQUATIONS OF LASER CONSOLIDATION

The laser beam, with radius r, moves at constant velocity v in the x-direction as it scans over the surface of the powder bed, which lies in the $(x,\, y)$ plane (Figure 3). It is represented by a Gaussian intensity distribution in the $(x,\, y)$ plane,

$$I(x, y, t) = \frac{A \cdot P}{\sigma\, \pi\, r^2} \exp\left(-\frac{(x - v\, t)^2 + y^2}{\sigma\, r^2} \right) \equiv I_0 \exp\left(-\frac{(x - v\, t)^2 + y^2}{\sigma\, r^2} \right), \tag{1}$$

where P is the power of the laser beam at the surface of the powder bed, A is the absorptivity of the powder, I_0 is the peak intensity of the beam, and σ describes the shape of the intensity distribution (Figure 4). For most SLM machines, r is measured at the position where the intensity of the beam has fallen to $1/\mathrm{e}^2$ of its maximum intensity, and therefore $\sigma = 2$. Assuming that the heat transfer is dominated by thermal conduction, the heat diffusion equation can be written as

$$\rho\, c_p \frac{\partial T}{\partial t} - \mathrm{Div}\,(k\, \mathrm{Grad}\, T) = I\,(x,\, y)\, \delta\,(z)\,, \tag{2}$$

where $\rho = \rho(T)$ is the mass density, $c_\mathrm{p} = c_\mathrm{p}(T)$ is the specific heat capacity, $k = k(T)$ is the thermal conductivity, and $\delta\,(z)$ is a delta function at the surface of the powder bed. The mechanical problem is described by balance of linear momentum written in the reference configuration,

$$\rho \frac{\partial^2 \mathbf{u}}{\partial t^2} - \mathrm{Div}\sigma = 0, \tag{3}$$

where $u = u(\mathbf{X}, t)$ is the displacement vector, and $\sigma = \sigma(\mathbf{X}, t)$ is the Cauchy stress tensor.

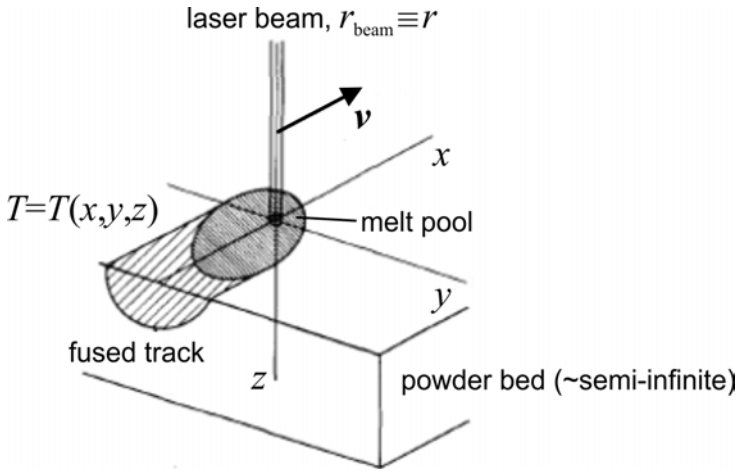

Figure 3. Schematic of the modeling of the laser fusion process. The laser beam moves at constant velocity in the x-direction, and the powder bed is approximated as semi-infinite. The model predicts the steady temperature distribution that moves with the beam at velocity $\mathbf{v}$.

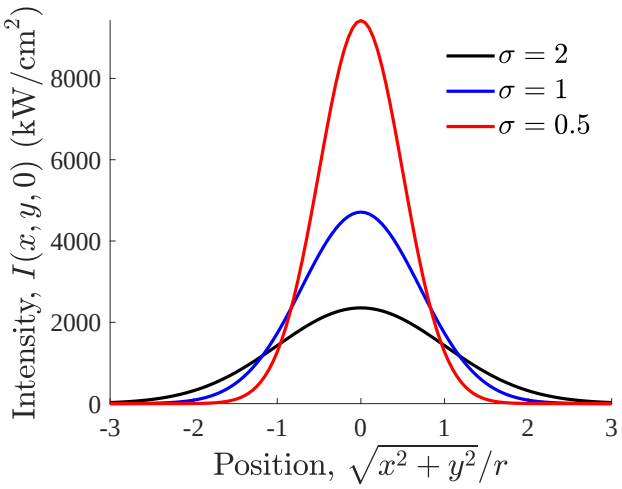

Figure 4. Profile of the laser beam intensity as a function of the radial position for various values of σ*, the beam shape parameter.*

4. ANALYTICAL MODELING OF LASER CONSOLIDATION

With the benefit of several modeling assumptions, we derived the analytical solution for the steady state temperature distribution generated by a scanning Gaussian intensity source. This analytical model serves two purposes: First, it identifies simple nondimensional groups of process parameters and material properties that affect the properties of the consolidated material. Second, it acts as a benchmark for the more complex numerical models of Section 5, verifying many aspects of the numerical methods.

We model the powder bed as semi-infinite and approximate the material properties to be independent of temperature. At steady state, the heat equation can be solved for $t = 0$, when the laser beam is at $x = 0$, by superimposing the Gaussian intensity distributions that occurred at earlier times $t' = 0 \rightarrow -\infty$ when the beam was located at coordinates (x', y'). The solution is found by by a standard Green's function method and then integrated analytically over x' and y'. Transformation to dimensionless variables results in

$$T(x, y, z) - T_0(x, y, z) = \frac{A \cdot P}{k\, r} \int_0^\infty \frac{\exp(-H)}{\sqrt{\sigma}\pi^{3/2}(1+u^2)} \mathrm{d}u, \tag{4}$$

with

$$H = H\left(\frac{x}{r}, \frac{y}{r}, \frac{z}{r}, \frac{v\, r}{\alpha}, \sigma, u\right), \tag{5}$$

in which u is a dimensionless function of $t'' \equiv -t'$. The solution therefore takes the form of an amplitude term that does not vary with position multiplied by a dimensionless shape function:

$$T(x, y, z) - T_0(x, y, z) = \underbrace{\frac{A \cdot P}{k\, r}}_{\text{dimension } T} \times \underbrace{f\left(\frac{x}{r}, \frac{y}{r}, \frac{z}{r}, \frac{v\, r}{\alpha}, \sigma\right)}_{\text{dimensionless shape function}}. \tag{6}$$

The amplitude term increases with increasing absorbed power and decreases with increasing thermal conductivity and beam size. The shape function, f, depends only on the shape of the beam's intensity profile and the dimensionless velocity, $\overline{v} \equiv v\, r/\alpha$, where $\alpha = k/\rho c_\mathrm{p}$ is the thermal diffusivity. The dimensionless velocity, also known as the Péclet number, characterizes the ratio of heat flow by transport to heat flow by diffusion. For a given thermal conductivity and beam intensity, f completely determines the distribution of temperature in the material. Similarly, a dimensionless group describing the power that is required for the laser melting of metals can be defined by dividing the amplitude term by the temperature rise: $\overline{P} \equiv \frac{A \cdot P}{k\, r} \frac{1}{(T_\mathrm{m} - T_0)}$.

We numerically integrate Equation 4 and evaluate the shape function along each of the coordinate axes to determine the maximum temperature in the material and explore the shape of the temperature distribution as a function of the dimensionless velocity (Figure 5). As expected, in the y and z directions, the temperature is a maximum at the center of the beam and at the surface of the material ($y = 0$, $z = 0$). However, in the x-direction, the maximum temperature shifts farther

behind the center of the beam as $\overline{v}$ increases (Figure 5a). As the beam velocity increases, the time for heat flow by conduction decreases, and the effect of heat input at prior times and locations begins to dominate over the effect of thermal conduction.

Considering a powder bed composed of plain AlSi10Mg (Table 1), we now integrate over the surface to solve for $T(x, y, z = 0)$ as a function of laser power and scan velocity. Maintaining a constant areal energy density, $E_{\mathrm{A}} \equiv P/(v \cdot 2r)$, we plot the predicted temperature distribution at three different powers and velocities (Figure 6). Here, although the energy density is the same in each case, the melt pool dimensions, aspect ratio, and peak temperature increase with increasing scan velocity. Referring to the temperature solution (Equation 6), we note that the amplitude term increases linearly with increasing laser power, but the effect of increasing the scan velocity is hidden within the shape function (which includes an exponential term). Because AlSi10Mg has a high thermal diffusivity, $\alpha = 6.2 \times 10^{-5}\,\mathrm{m}^2/\mathrm{s}$, $\overline{v}$ is small at these scan velocities, ranging from $v\,r/\alpha = 0.32$ to $v\,r/\alpha = 1.28$. Therefore, as shown in Figure 6, the shape function hardly changes as the scan velocity increases in this range. With the amplitude term increasing linearly and the shape function remaining approximately constant, the temperature and thus the melt pool dimensions must increase as the laser power is increased at constant energy density.

The key result of this analysis is the nonlinear relationship between $\overline{v}$ and the distribution of temperature in the material. At constant laser intensity, when $\overline{v}$ decreases in the range of $\overline{v} = 1{-}100$, the maximum temperature in the material increases logarithmically, but thereafter there is little benefit in increasing $\overline{v}$. Similarly, the size of the melt pool, indicated by the width of the temperature distributions at a given value of f, does not increase significantly for $\overline{v} \lesssim 1$. This result explains the limitations in laser consolidation of increasing energy density by decreasing laser scan velocity. Rather, it is preferable to increase laser power, particularly for materials with high thermal diffusivity, such as aluminum alloys.

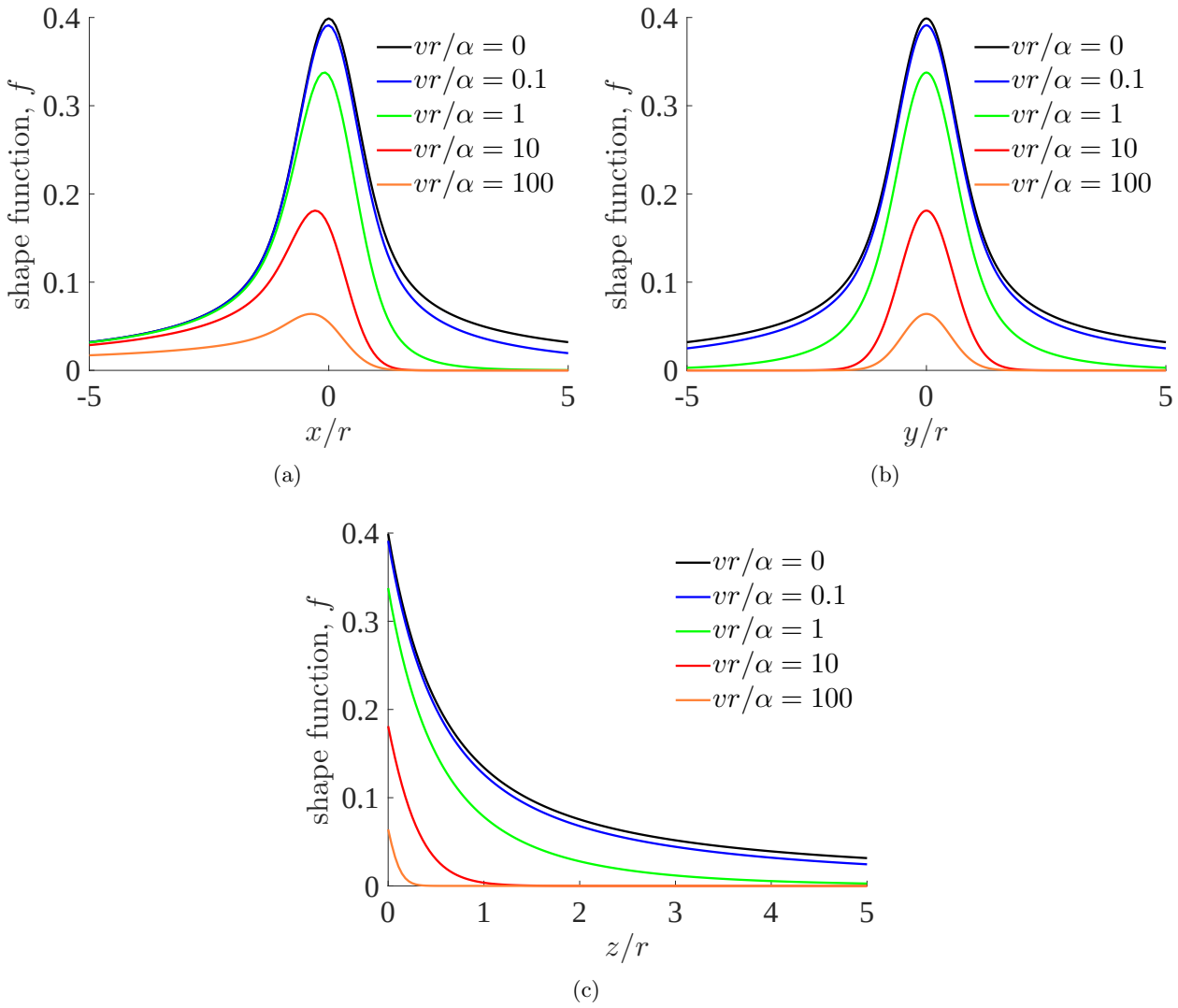

Figure 5. Plots of the shape function f that predicts the distribution of temperature in the powder bed as a function of dimensionless velocity, $\overline{v} = v\,r/\alpha$. (a) Along the x-axis, the direction of laser travel, the peak temperature lags behind the location of the beam ($x = 0$). (b) Along the y-axis, the temperature distribution is symmetric. (c) Along the z-axis, f predicts the depth of penetration of the temperature disturbance. As $\overline{v}$ decreases, f and thus the temperature distribution approach constant profiles.

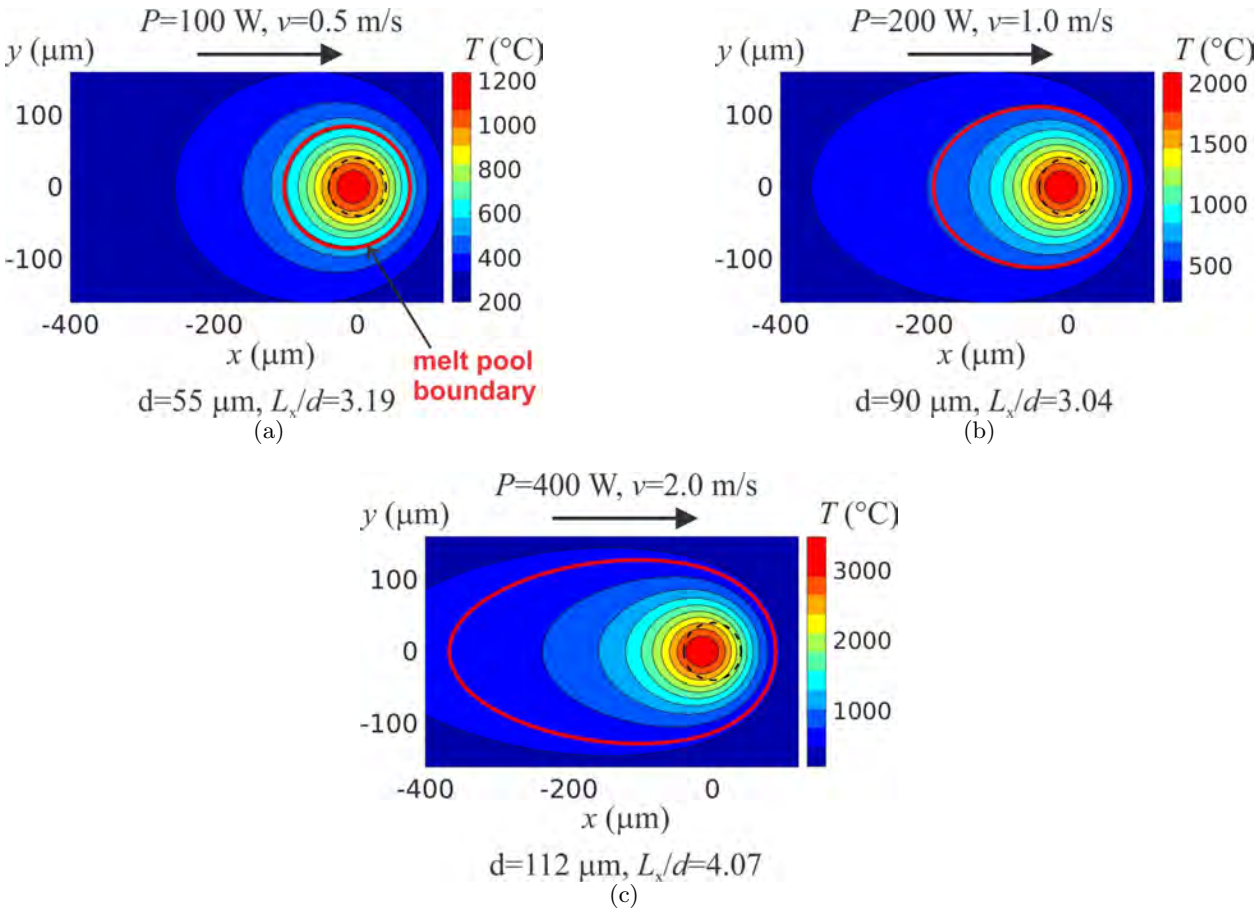

Figure 6. Analytical model predictions of melt pool size and temperatures $T(x, y, 0)$ for plain AlSi10Mg: melt pool dimensions, aspect ratio, and maximum temperature increase with increasing laser scan velocity at constant areal energy density, E_A (for $d_{beam} = 80$ μm and $A = 0.35$). (a) $v\,r/\alpha = 0.32$. (b) $v\,r/\alpha = 0.64$. (c) $v\,r/\alpha = 1.28$. (Dashed circle indicates position of laser beam spot.)

TABLE 1

Physical Properties of AlSi10Mg

Powder density, ρ_{pow}	$1300\,\text{kg/m}^3$
Consolidated density, ρ_{dens}	$2670\,\text{kg/m}^3$
Powder thermal conductivity, k_{pow}	$10\ \text{W/m K}$
Consolidated thermal conductivity, k_{dens}	$150\ \text{W/m K}$
Specific heat c_{p},	$900\ \text{J/kg K}$
Thermal diffusivity, α (calculated)	$1.28 \times 10^{-5} - 6.25 \times 10^{-5}\,\text{m}^2/\text{s}$
Solidus temperature, T_ℓ	$558\,^\circ\text{C}$
Liquidus temperature, T_{s}	$594\,^\circ\text{C}$
Vaporization temperature, T_{v}	$2450\,^\circ\text{C}$
Latent heat of fusion, L_{f}	$389\,\text{kJ/kg}$
Effective absorptivity, A	0.35

This page intentionally left blank.

5. NUMERICAL MODELING OF LASER CONSOLIDATION

Analytical models and nondimensional groups can uncover fundamental relationships between process parameters, microstructure, and properties, but it is very difficult to derive analytical solutions for cases with finite geometry or modes of heat transfer in addition to pure conduction. On the other hand, numerical solutions can predict melt pool characteristics and thermal history under conditions far more complex than those of the idealized case of Section 4. Some of the phenomena that can readily be incorporated into numerical models are convective heat transfer, thermal radiation, phase changes, temperature dependence of material properties, and multiple scan tracks.

In the numerical solutions, the material is modeled at the continuum level, where the computational cost is reasonable, using the finite element method to solve the heat and momentum equations. Although models of SLM have been proposed in the literature, there is still a critical need for comprehensive, numerically efficient models that capture the coupled physics of heat transfer and deformation. Reviewing the prior work, we identified opportunities in the following areas, among others:

- Efficient numerical schemes: adaptive time stepping, optimized element sizes, element activation, and elements with hybrid shape functions for u and T that are not prone to locking
- Realistic material models for compaction of powder and viscoplasticity of the solidified metal at elevated temperature
- Physical representations of melt pool convection and recoil pressure based on non-local field variables defined by dimensional analysis
- Benchmarking of numerical methods and modeling assumptions with analytical solutions and the results of experiments
- Massive parallelization using resources at the LL Supercomputing Center

Our objective was to develop accurate, efficient models of the heat transfer process. To this end, first, the analytical solution of Section 4 was derived. Then, a numerical model of the pure conduction problem was built for solution by the commercial finite element solver Abaqus (Dassault Systemes). In the numerical model, the intensity of the laser beam is described by the same Gaussian form previously given by Equation 1. The preprocessing and postprocessing of all numerical simulations were scripted in Python so that parametric studies could be readily performed. With this capability, we can easily run multiple simulations in order to identify trends associated with single or groups of process parameters. As such, the detailed physics of SLM can be simulated nearly as easily as they can be with an analytical model.

5.1 NUMERICAL INTEGRATION SCHEMES

A critical step in developing a numerical model is to determine a domain size and level of discretization that provide an optimum balance between accuracy and computational cost. In general, these parameters depend on the properties of the material being modeled, and here we focus on AlSi10Mg (with physical properties given in Table 1). In these initial numerical simulations, the material properties are approximated to be independent of temperature and the effects of phase changes are neglected so that the predictions can be directly compared with those of the analytical model. For process parameters, we select the typical parameters used for AlSi10Mg with an EOS M 290 SLM machine (Table 2).

TABLE 2

Typical SLM Process Parameters for AlSi10Mg

Laser power, P	370 W
Laser scanning speed, v	1.3 m/s
Layer thickness, t	40 μm (effective)
Beam radius, r	50 μm
Hatch spacing, h	190 μm
Initial temperature, T_0	20 °C

For AlSi10Mg, parametric studies of single track consolidation were carried out to determine the optimum geometry of the simulation domain and the appropriate number of solution points within this domain. Based on the analytical predictions of the size of the heat-affected zone, the domain size was chosen to be $L_x = 1.52$ mm, $L_y = 0.8$ mm, and $L_z = 0.4$ mm (Figure 7). This domain was discretized with eight-node linear heat transfer elements (Abaqus DC3D8). Simulating single track consolidation with decreasing element size, we found that the analytical solution for the steady state temperature distribution could be matched with an element size of $h \approx 20$ μm, or about one-fifth of the diameter of the laser beam (Figure 8a). Furthermore, with this element size, the transient numerical solution approaches the steady state analytical solution after a scan length of only $L_{\text{scan}} = 0.60$ mm (Figure 8b), verifying that the overall length of the domain, L_x, is sufficient. Considering the size of the heat-affected zone (Figure 7), we estimate that the width and depth of the domain could each be decreased in size by about 33%. Summarizing the spatial requirements, a domain volume of about 0.25 mm^3 and about 14,000 linear finite elements are adequate to simulate single track consolidation of AlSi10Mg under typical SLM conditions.

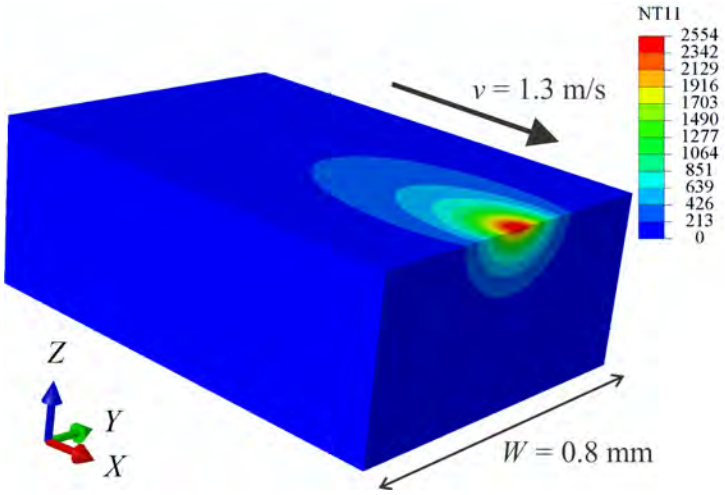

Figure 7. Numerical simulation of single track consolidation of plain AlSi10Mg at scan length $L_{\text{scan}} = 0.6\,mm$ ($P = 370\,\text{W}$, $v = 1.3\,\text{m/s}$, $d_{\text{beam}} = 100\,\mu m$, $A = 0.35$, and element size $h = 10\,\mu m$).

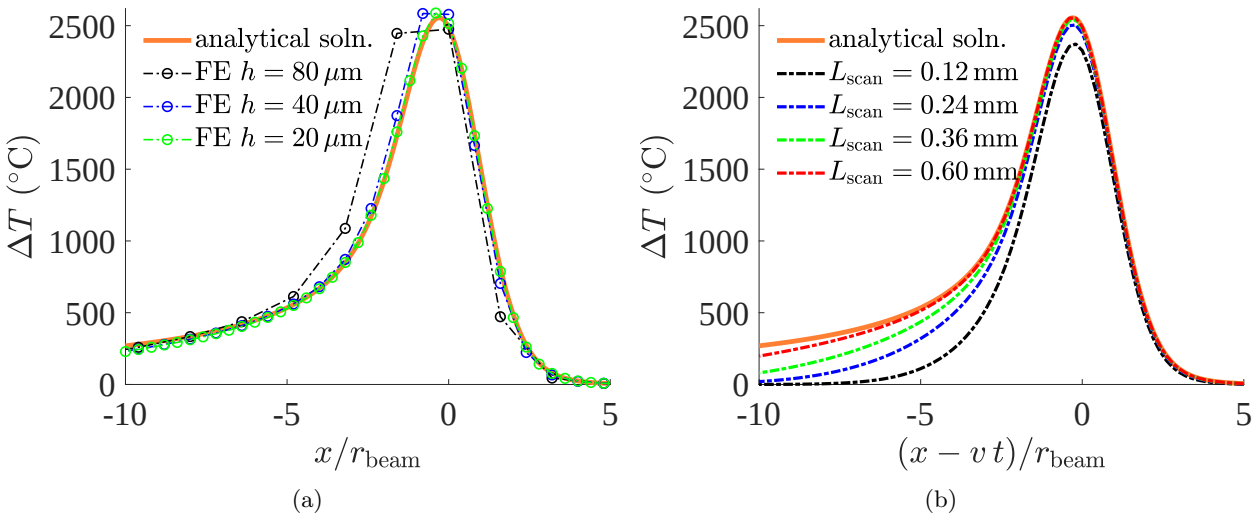

Figure 8. Comparison of the melt pool temperatures predicted by analytical and numerical models as a function of (a) element size and (b) laser scan length. Steady state analytical solution is approached at $h = 20\,\mu m$ and $L_{\text{scan}} = 0.60\,mm$.

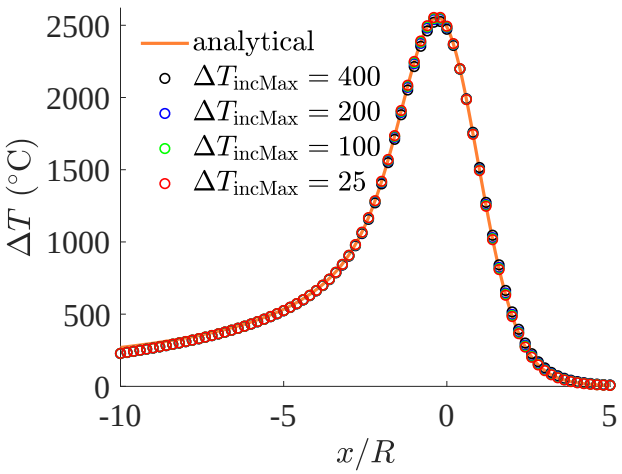

Figure 9. Comparison of the melt pool temperatures predicted by analytical and numerical models as a function of the size of the time increment used in the time integration scheme. Time increments that allowed the temperature to change by as much as 400 °C still produced an accurate solution ($h = 20\,\mu m$, $L_{\text{scan}} = 0.72\,mm$).

Like the spatial integration scheme, the time integration scheme was also optimized in order to minimize solution time. In another parametric study, with $h = 20$ μm and $L_{\text{scan}} = 0.72$ mm, the effect of increasing the maximum incremental temperature change was investigated. The results show that the time increment can be increased to a length that allows changes in temperature as long as $\Delta T_{\text{incMax}} = 400\,^{\circ}\text{C}$ during a single time increment, without significantly affecting the prediction of the steady state temperature distribution (Figure 9). This time increment reduces the total simulation time by a factor of 12, compared to the time increment corresponding to the initial guess of $\Delta T_{\text{incMax}} = 25\,^{\circ}\text{C}$.

5.2 ALGORITHM FOR MATERIAL PHASE CHANGES

With the numerical solution methods benchmarked and optimized, the numerical model was extended to capture changes of material phase. At each time step in the simulation, the material at each integration point in the domain is described by three state variables: the material phase (powder, consolidated solid, or liquid metal), the volume fraction of dense material (including both liquid and consolidated solid), and the maximum temperature at that point during the current total simulation time (Table 3). AlSi10Mg, like most alloys, melts and solidifies over a range of temperature called the "mushy" zone, $T_{\text{s}} \leq T \leq T_{\ell}$, where T_{s} is the solidus temperature and T_{ℓ} is the liquidus temperature. The material therefore melts and solidifies gradually, avoiding the numerical instability that would occur if the change of phase happened abruptly at a single temperature. The

volume fraction of dense phase is given by

$$\phi = \begin{cases} 0 & \text{if} \quad T \leq T\text{s}, \\ \dfrac{T - T_\text{s}}{T_\ell - T_\text{s}} & \text{if} \quad T_\text{s} < T < T_\ell, \\ 1 & \text{if} \quad T \geq T_\ell, \end{cases} \tag{7}$$

under the constraint $\dfrac{\mathrm{d}\,\phi}{\mathrm{d}\,T} \geq 0$ because densified material, whether liquid or solid, cannot spontaneously transform back to powder. Initially, before the arrival of the laser beam, the material is powder (iPhase=1), but, when the temperature exceeds T_ℓ, it changes to liquid (iPhase=3). Once the material is liquid and the temperature then decreases below T_s, the liquid transitions to consolidated solid (iPhase=2).

TABLE 3

Variables in Numerical Model Describing Material State

State variable	**Description**	**Values**
iPhase	Material phase	1 – Powder 2 – Consolidated solid 3 – Liquid
ϕ	Volume fraction of dense phase	$0 - 1$
T_max	Maximum temperature reached at material point	$T_0 - \infty$

Associated with the phase changes are latent heat effects and the dependence of the material properties on temperature. The latent heat of fusion is incorporated by increasing the specific heat capacity when the temperature is between T_s and T_ℓ:

$$c_\text{p} = \begin{cases} c_\text{p,sensible} & \text{if} \quad T \leq T\text{s}, \\ c_\text{p,sensible} + \dfrac{L_\text{f}}{T_\ell - T_\text{s}} & \text{if} \quad T_\text{s} < T < T_\ell, \\ c_\text{p,sensible} & \text{if} \quad T \geq T_\ell. \end{cases} \tag{8}$$

The thermal conductivity and mass density of the material are related to the temperature through their dependence on the volume fraction of dense phase:

$$k = k_{\text{pow}} \; + \; \phi \times (k_{\text{dens}} - k_{\text{pow}}) \,, \tag{9}$$

and

$$\rho = \rho_{\text{pow}} \; + \; \phi \times (\rho_{\text{dens}} - \rho_{\text{pow}}) \,, \tag{10}$$

where $k_{\text{pow}} \ll k_{\text{dens}}$ and $\rho_{\text{pow}} \approx 1/2\, \rho_{\text{dens}}$ (Table 1).

5.3 PREDICTIONS OF THE NUMERICAL MODEL WITH MATERIAL PHASE CHANGES

Adding these effects to the numerical model significantly changes the distribution of temperature and the dimensions of the melt pool (Figure 10). Here, we simulated a 40 μm layer of AlSi10Mg powder spread on a build plate of AlSi10Mg. The low thermal conductivity of the powder surrounding the heat-affected zone insulates the melt pool, causing the melt pool to increase in size and temperature, relative to the predictions of the simulation without phase changes. Similarly, the insulating effect of the powder decreases the width of the heat-affected zone and reduces its extent in the scan direction. Conversely, the length of the tail of the heat-affected zone increases because the consolidated material left in the wake of the melt pool has high thermal conductivity (Figure 11).

As a whole, the predictions of the numerical model are consistent with the formation of stable melt pools and the consolidation of defect-free parts. The predicted melt pool measures about 380 μm long, 160 μm wide, and 100 μm deep. A melt pool of these dimensions is expected to be stable because it avoids the capillary instability that occurs in liquid cylinders with $L/d > \sqrt{3/2}\,\pi$. Furthermore, it is also deep enough to remelt over 50 μm of the build plate, ensuring a good connection between the layers in a build. The maximum temperature predicted, about 2700 °C, exceeds the vaporization temperature of aluminum, indicating that the metal will vaporize at the surface of the melt pool. However, vaporization is common in SLM and is not a concern unless it causes a significant change in the elemental composition of the alloy.

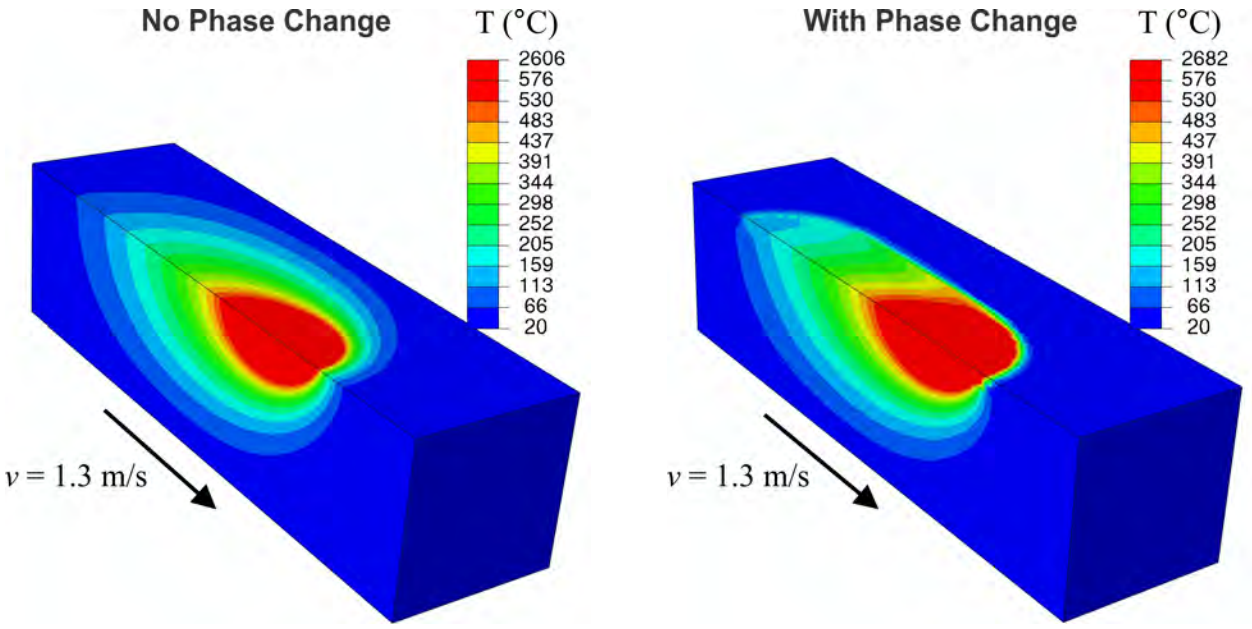

(a) (b)

Figure 10. Numerical simulations showing the effect of material phase changes and the temperature dependence of material properties on the prediction of the steady state temperature distribution for AlSi10Mg. The phase changes and accompanying change in material properties increase the melt pool temperature and dimensions, but they decrease the size of the heat-affected zone ($h = 20\,\mu m$, $L_{\text{scan}} = 0.72\,mm$).

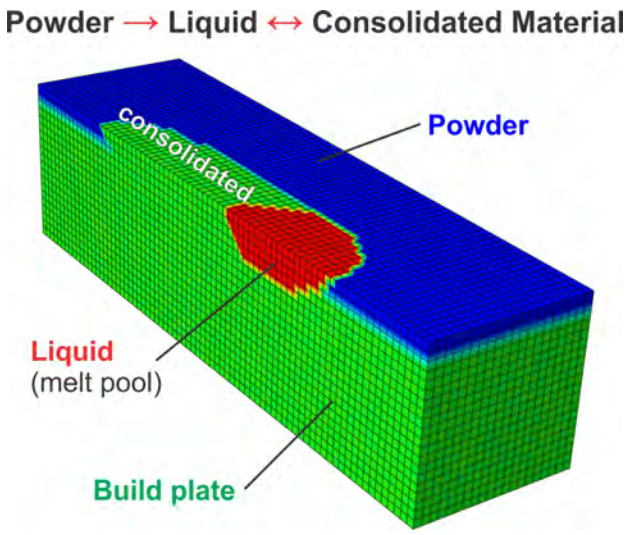

Figure 11. Distribution of material phases for the simulation of AlSi10Mg shown in Figure 10 ($h = 20\,\mu m$, $L_{\text{scan}} = 0.72\,mm$).

6. EXPERIMENTAL VALIDATION: SINGLE TRACK CONSOLIDATION EXPERIMENTS

The research in FY19 focused on acquiring experimental data that could be used to validate the modeling and identify its shortcomings. Therefore, we performed single track consolidation experiments on both plain and ceramic-reinforced aluminum alloys.

The laser consolidation was performed with a custom-built SLM testbed from Aconity3D in Germany (Figure 12). Unlike commercial machines, the SLM testbed allows selection of process parameters over a wide range of laser parameters, scan strategies, powder bed temperatures, and recoating parameters. In the development of new alloys and composites, the selection of these parameters will be guided by the analytical and numerical models described in the previous sections. These models will be used to predict melt pool characteristics and thermal history as a function of process parameters and powder composition. The process parameters will then be tuned to produce desirable microstructures and prevent the occurrence of defects.

6.1 DESCRIPTION OF SLM TESTBED

The SLM testbed is an open access system designed to MIT LL specifications for the development of new materials for SLM. Its key features include:

- Inert build chamber with recirculation and filtering that enable the processing of highly reactive materials such as aluminum alloys. (Flow rate of inert gas across the build plate is controlled to remove weld fumes and splatter.)
- Continuous wave fiber laser with maximum power of 420 W
- Full control of the laser scan path
- Powder bed preheating up to 500 °C
- Interchangeable recoater blade (steel, rubber, or carbon fiber brush) and full control of powder layer thickness, blade height, and blade velocity
- Melt pool temperature sensing with two pyrometers
- High speed CMOS camera
- Support for additional sensors for process monitoring and addition of feedback control

6.2 LASER CONSOLIDATION OF SINGLE TRACKS OF POWDER

In these experiments, single lines of AlSi10Mg powder (LPW) and Al-TiB_2 powder fabricated at MIT LL were consolidated with the SLM testbed at various laser powers and scan velocities.

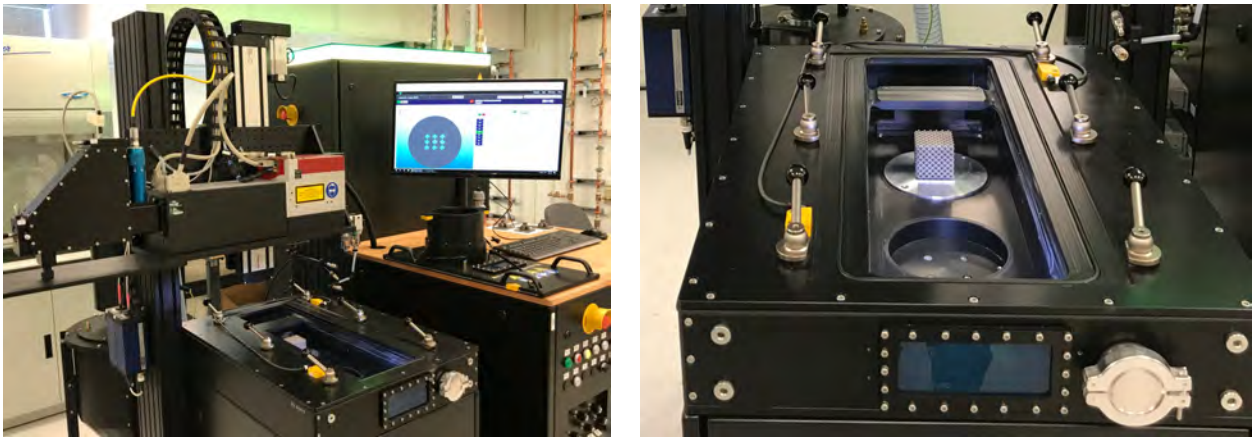

(a) (b)

Figure 12. Aconity SLM research testbed. (a) Build chamber, CW fiber laser, scan head, and control cabinet. (b) Close-up of build chamber, showing powder supply cylinder, build platform, and powder recoater (front to back).

This type of experiment is a highly efficient way to estimate the range of process parameters that can be used to fabricate bulk samples with minimal defects. Within this process window, the single lines, or tracks (similar to laser weld beads), exhibit the following characteristics:

- Smooth, uninterrupted profiles when viewed from above
- Sufficient penetration into the substrate to ensure a strong connection
- Sufficient height above the substrate to build in the vertical direction
- An angle of connection with the substrate of close to 90°

In addition to the determination of laser power and scan velocity, single track experiments can also provide estimates of the optimal hatch spacing and powder layer thickness, based on the dimensions of the weld bead's profile.

We prepared single layer samples by spreading 75 μm layers of gas atomized and composite powder over an AlSi12 substrate using the SLM recoater equipped with a metal blade. Single lines of powder were then consolidated at powers of 95–380 W and scan velocities of 50–2000 mm/s. The scan lines were all 7.5 mm long and were spaced at 1.5 mm intervals.

The consolidated tracks were characterized extensively with both light microscopy and scanning electron microscopy (SEM). First, the width of the tracks was measured at multiple locations

in order to determine the characteristic width of the melt pool under the corresponding process parameters. Then, the AlSi12 plate was sectioned with a diamond saw at about the midpoint of each set of track. One half of each row of tracks was then ground flat with silicon carbide abrasive papers and polished with diamond slurries so that the width and depth of the melt pool could be measured also in the perpendicular plane.

The results of these experiments show that the process window for plain AlSi10Mg comprises laser powers of about 200–400 W at velocities that increase with increasing laser power (Figure 13). Outside this window, at high powers and low velocities, the melt pool transitioned from conduction mode to keyhole mode. In keyhole mode, the melt pool temperature exceeds the alloy's boiling point, and evaporation of the liquid metal and high vapor pressures cause a deep channel to form within the melt pool. After the laser passes, the molten metal fills in the channel, leaving behind a flat weld bead and often pores where the channel did not fully close ("keyhole pores," as shown in Figure 13, left). On the other hand, outside the window at low powers and high velocities, the weld bead exhibits irregularities and poor connection to the substrate (Figure 13, right). Here, the melt pool failed to wet the substrate completely because surface tension spheroidized the liquid and the substrate did not melt sufficiently.

The complete set of plain AlSi10Mg tracks (Figures 14 and 15) was characterized from both views, and the results were compared with the predictions of the numerical simulations (Figure 16). The results of the simulations show that the numerical model correctly predicts the trends of decreasing melt pool size with both increasing laser scan velocity and decreasing laser power. However, whereas the measurements and model predictions are reasonably close to each other, the model does significantly overpredict the dimensions of the melt pool. This disparity occurs because the model does not presently capture the effects of melt pool convection and keyholing, two mechanisms that transfer heat away from the laser spot location to regions below the surface and behind the laser.

Additional single track consolidation experiments were performed on composite powders fabricated at MIT LL with planetary ball milling. In these experiments, AlSi10Mg powders reinforced with 10–30 wt% titanium diboride were consolidated in single tracks (Figures 17–19). Because the laser absorptivities of non-oxide ceramics such as titanium diboride are much higher than that of aluminum, the absorbed laser powder should significantly increase with increasing ceramic content, and we would expect the widths of the consolidated tracks to increase with increasing ceramic content. However, the consolidated tracks in fact became narrower as the ceramic content of the powder increases. We hypothesize that the unmelted ceramic particles suspended in the melt pool increased the melt pool viscosity and therefore decreased the spreading of the melt pool over the substrate. For this reason, the numerical model becomes increasingly inaccurate as the ceramic content of the powder increases.

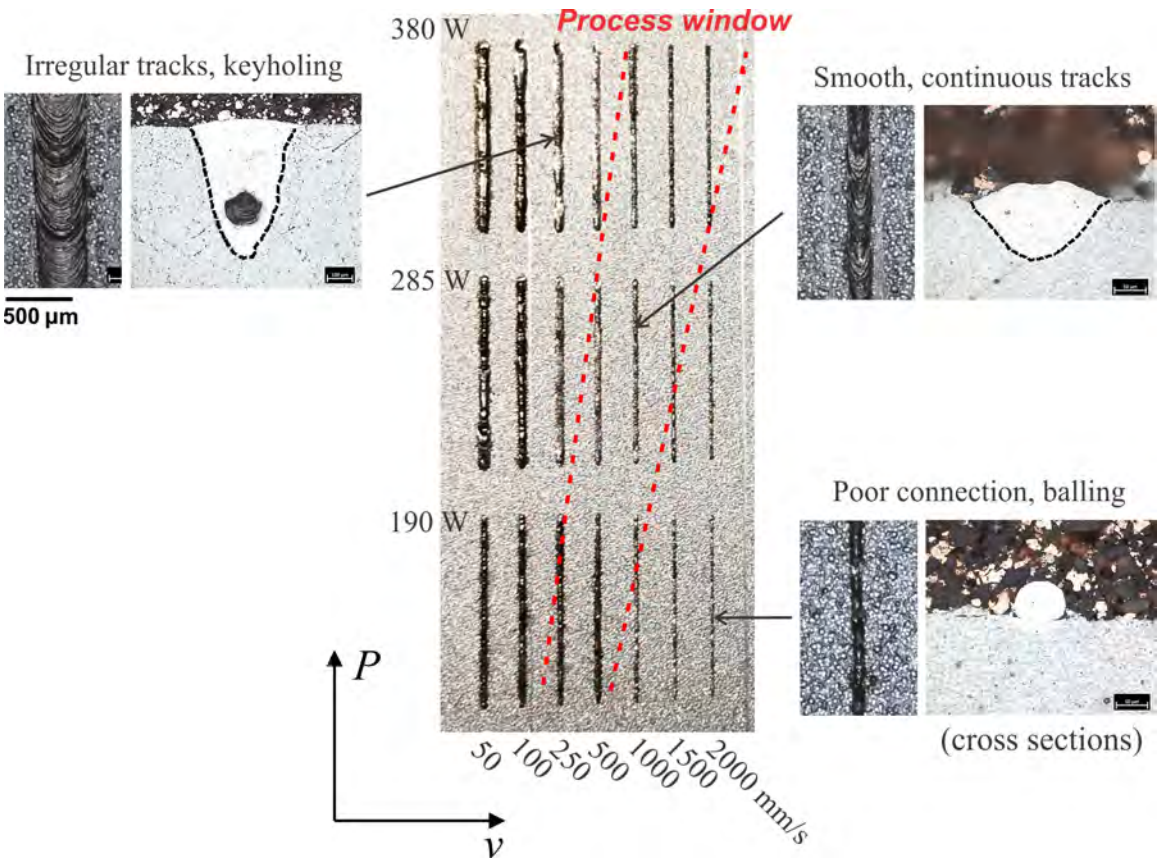

Figure 13. Process window for plain AlSi10Mg powder determined from single track melting experiments (75 µm powder layer spread on AlSi12 substrate).

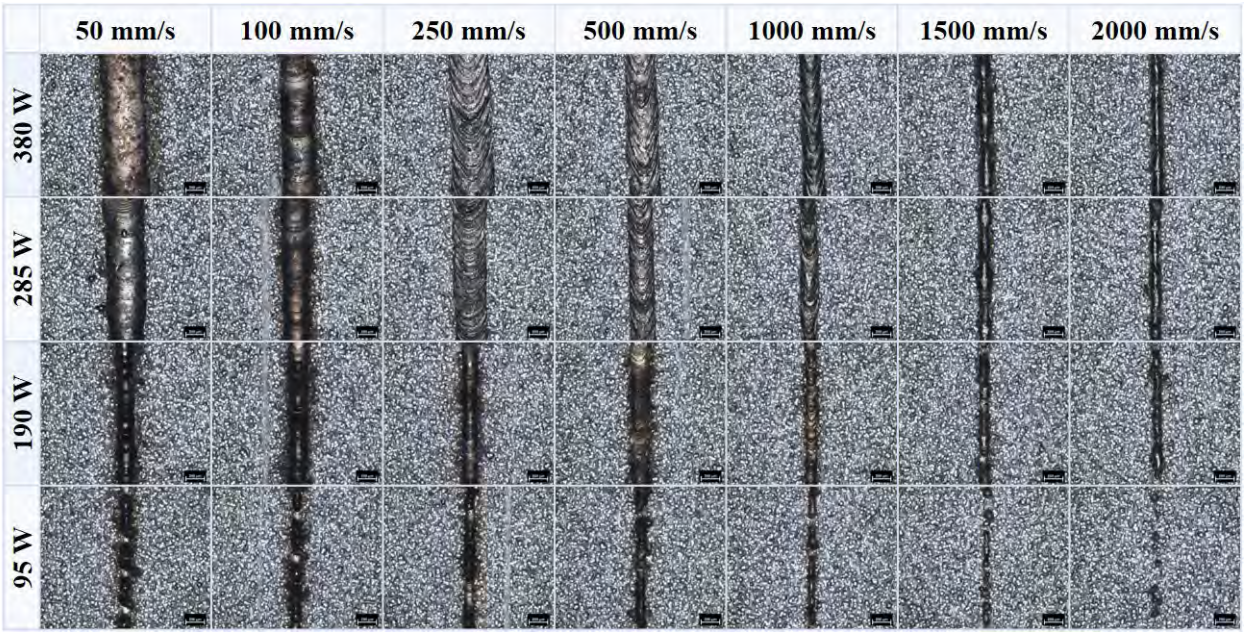

Figure 14. Top view of consolidated tracks of plain AlSi10Mg powder.

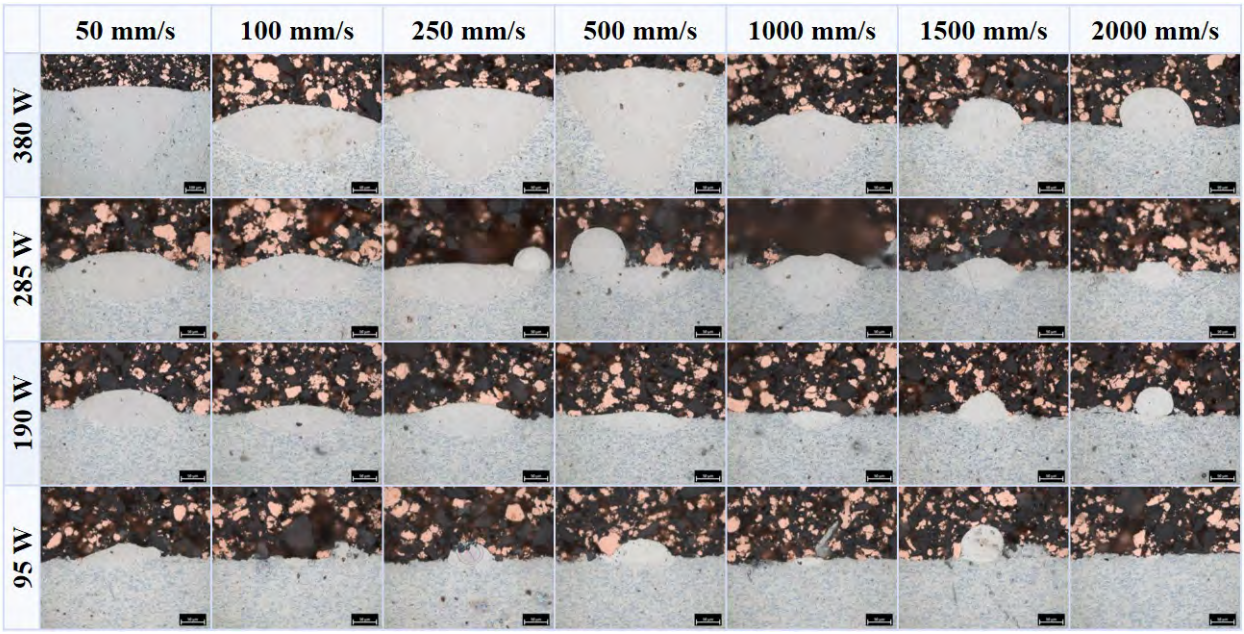

Figure 15. Section view of consolidated tracks of plain AlSi10Mg powder.

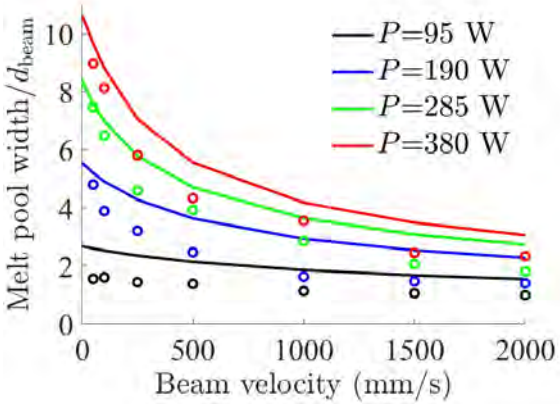

Figure 16. Melt pool widths during single track consolidation of plain AlSi10Mg powder: Numerical model predictions (solid lines) compared with experimental results (open circles).

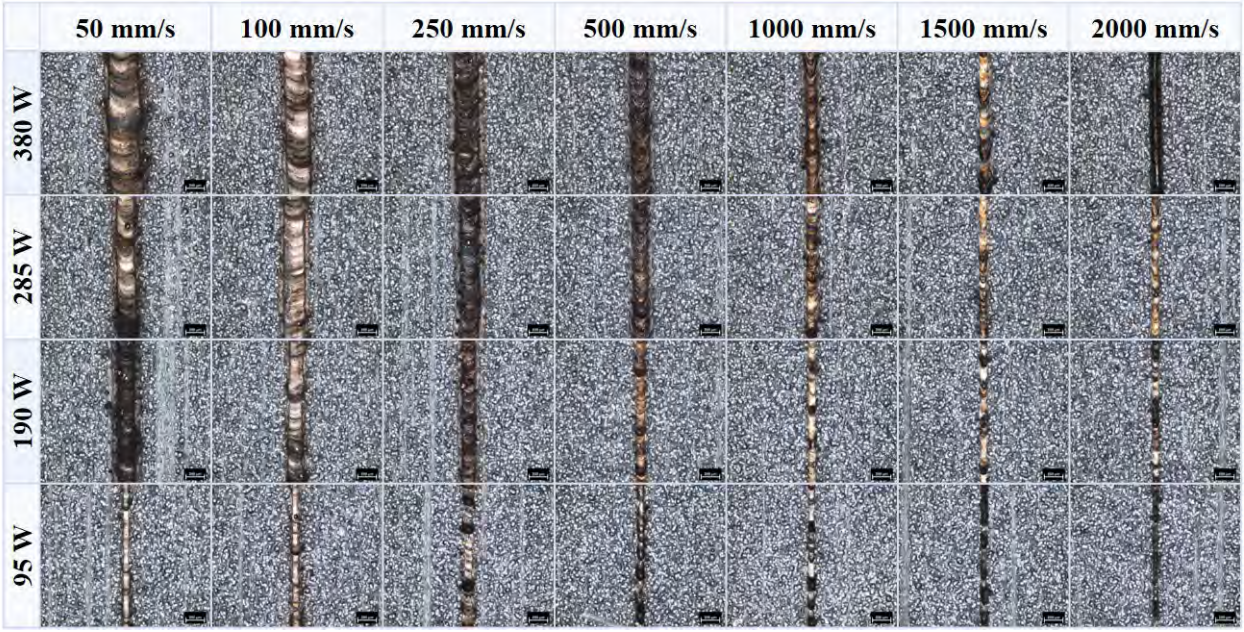

Figure 17. Single track consolidation of composite powder with $w = 10\%$, demonstrating the relationship between laser parameters and melt pool characteristics, as a function of powder properties.

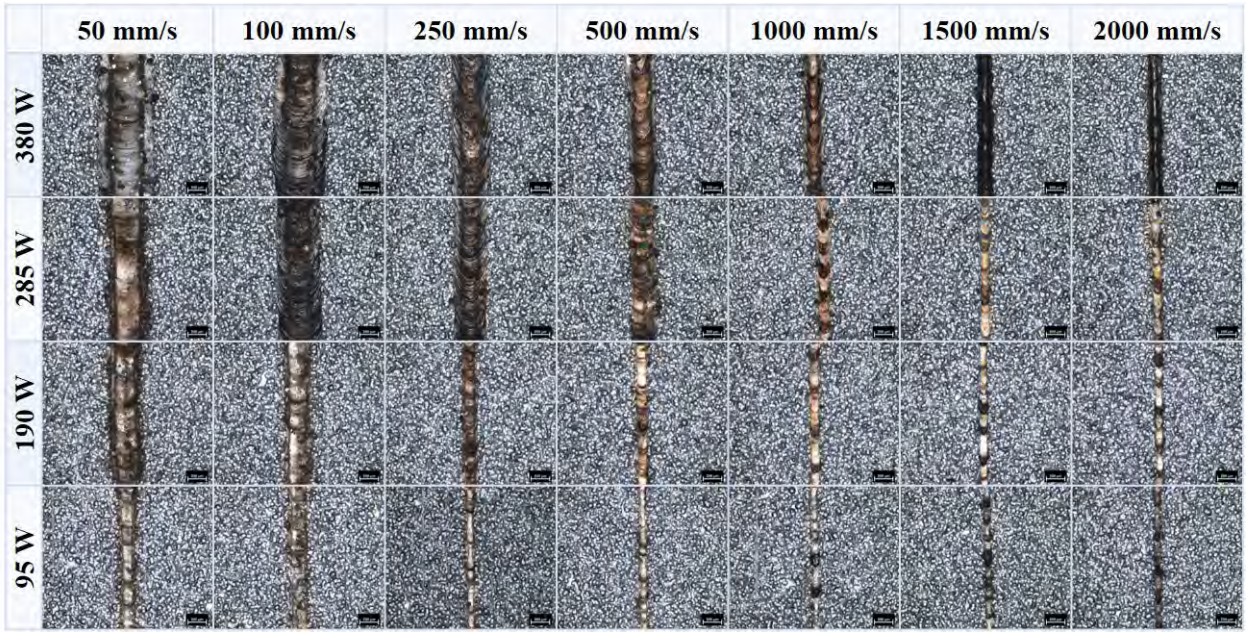

Figure 18. Single track consolidation of composite powder with $w = 16\%$, demonstrating the relationship between laser parameters and melt pool characteristics, as a function of powder properties.

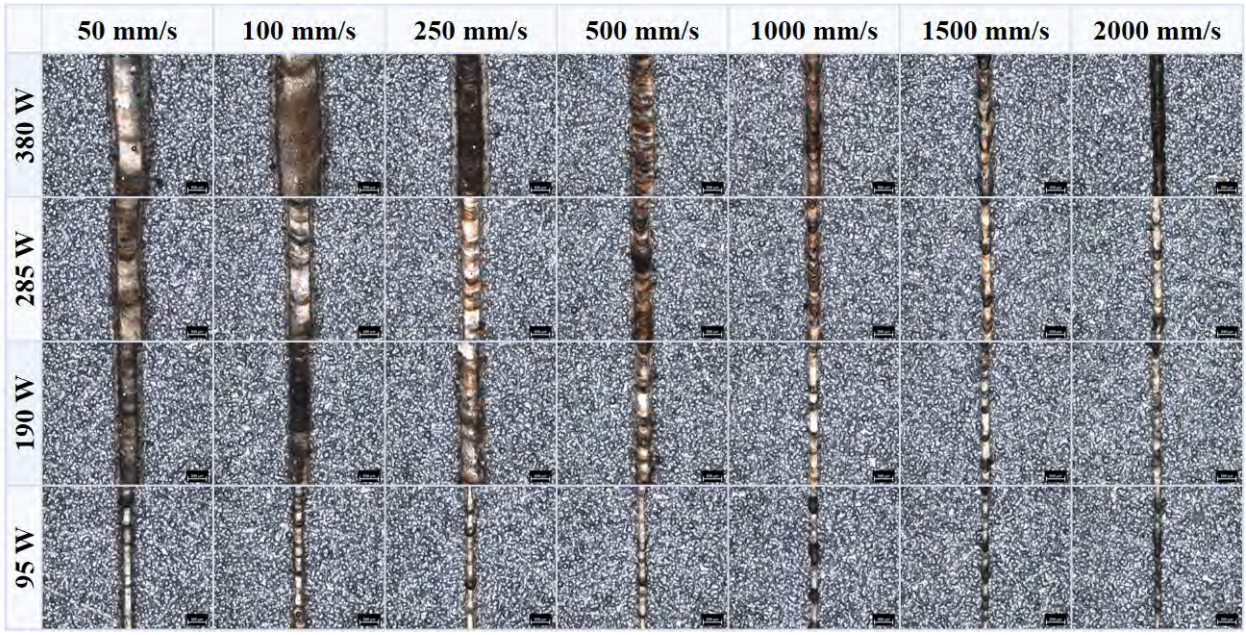

Figure 19. Single track consolidation of composite powder with $w = 30\%$, demonstrating the relationship between laser parameters and melt pool characteristics, as a function of powder properties.

7. EXTENSIONS OF THE MODEL TO CAPTURE ADDITIONAL MODES OF HEAT TRANSFER

In order to increase the accuracy of the numerical model, we are extending the model to capture the effects of melt pool convection and keyhole melting, as a function of the powder properties. After conduction, these are the two most important modes of heat transfer during selective laser melting.

Melt pool convection is driven by gradients of surface tension. As shown in the previous sections, the melt pool is hottest near the center of the laser spot and becomes gradually cooler as the distance from the laser spot increases. Because the surface tension of molten aluminum increases with decreasing temperature, the surface tension is higher near the boundaries of the melt pool than it is at the center of the melt pool. This gradient of surface tension causes the liquid metal to circulate front to back, producing a melt pool that is longer, deeper, and narrower than it would be without convection (Figure 20).

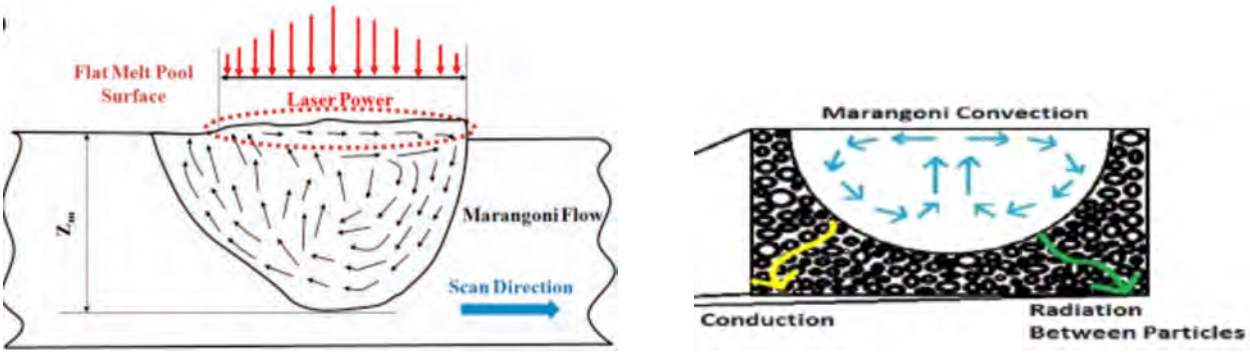

(a) (b)

Figure 20. Melt pool convection driven by the Marangoni effect.

Keyhole melting occurs at high energy densities when the temperature of the melt pool exceeds the vaporization temperature of the alloy. When the molten metal begins to evaporate, the rapidly expanding vapor exerts pressure on the melt pool (recoil pressure), causing a channel, or keyhole, to form in the melt pool at the location of the laser spot. Within the keyhole, the laser is repeatedly reflected and partially absorbed, such that virtually all of the beam's energy is absorbed by the melt pool. The result is a very deep, narrow melt pool (Figures 13 and 15).

We proposed to model these modes of heat transfer using an effective, anisotropic thermal conductivity tensor:

$$\kappa_{\text{eff}} = \kappa_{\text{eff}} \left(\mathbf{x}_{\text{beam}}, T, Ma, \mu \right), \tag{11}$$

where x_{beam} is the position vector relative to the center of the laser spot, Ma is the dimensionless Marangoni number that characterizes the strength of the melt pool convection,

$$Ma = -\frac{\mathrm{d}\,\gamma}{\mathrm{d}\,T} \frac{\Delta T\, w_{\text{melt}}}{\mu\, \alpha}, \tag{12}$$

$\frac{\mathrm{d}\,\gamma}{\mathrm{d}\,T}$ is the gradient of surface tension with respect to temperature, and $\mu = \mu\left(T\right)$, the temperature-dependent viscosity, can also depend on the volume fraction of ceramic reinforcement:

$$\mu = \mu_0 \left(\frac{1 - f}{f_{\max}} \right)^{-2}. \tag{13}$$

Because the thermal conductivity is no longer homogeneous, the heat equation is now written as

$$\rho\, c_p \frac{\partial T}{\partial t} - \operatorname{Div}\left(\kappa_{\text{eff}} \operatorname{Grad} T \right) = I\left(x,\, y\right) \delta\left(z\right), \tag{14}$$

which requires the derivatives of the thermal conductivity tensor to be evaluated. In this equation, the thermal conductivity tensor will be defined based on the current properties of the molten metal and the melt pool, including temperature, viscosity, surface tension, ceramic content, and melt pool dimensions.

Modeling melt pool convection and keyhole melting requires an unconventional approach because the physics are nonlocal. At each integration point, the response of the material depends, not only on the field variables at that location, but also on field variables at neighboring locations. The nonlocal field variables characterize the temperature gradient across the melt pool, the melt pool dimensions, and the shape of the keyhole. Therefore, a custom, portable user finite element was developed using the Abaqus/Stadard UEL interface (Figure 21). Within the element, the interpolation functions, residual flux vector, and Jacobian matrix are defined. The global system of equations is then assembled and solved with Newton's method. The user finite element was benchmarked with a heat transfer element from the Abaqus library, and we explored methods to evalulate and update the nonlocal terms in a computationally efficient manner. Because the Abaqus postprocessor does not have access to variables evaluated at integration points, we also developed an algorithm for plotting these output variables using dummy elements and global variables defined within an additional Abaqus subroutine (UMAT).

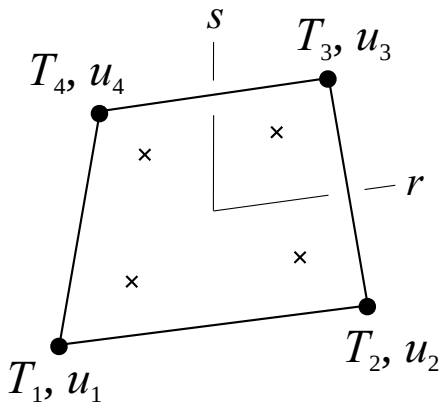

Figure 21. Finite element used to solve the heat equation with an anisotropic, inhomogeneous conductivity tensor.

This page intentionally left blank.

8. CONCLUSION

In this Technology Investment Program, we developed accurate, efficient models of the heat transfer and phase changes that occur during selective laser melting. First, the exact analytical solution was derived for the steady state temperature distribution generated by a scanning Gaussian intensity source. Next, a numerical model of the conduction problem, scripted for parametric studies, was developed and verified with the analytical solution, and the effects of model size, scan length, element size, and time step were investigated. Surprisingly, we found that the analytical solution can be approximated numerically with an element size as large as about one-quarter of the beam diameter and model dimensions on the order of 1 mm. The numerical model was then extended to simulate more detailed physics, including phase changes and temperature dependence of material properties. Agreeing with our intuition, these effects increased the temperature and dimensions of the melt pool, and the predictions were consistent with the melt pool characteristics of successful SLM builds.

This year, single track laser consolidation experiments were performed over wide ranges of laser power, scan velocity, and powder properties. The numerical model predictions and experimental results exhibited reasonable agreement, but the model systematically overpredicted the width of the melt pool. The disagreement occurred because the model did not adequately characterize melt pool convection and keyhole melting. Methods to model these additional modes of heat transfer were identified, and substantial progress was made toward developing and implementing the solution algorithms.

Although this Technology Investment Program concluded at the end of FY19, the modeling will continue as part of a Line-Supported Program in which aluminum metal matrix composites are being developed for selective laser melting. The predictions of the modeling will be critical for determining the process parameters for these new materials and relating the process parameters to the observed solidification microstructures. Process parameters will then be tuned to prevent the occurrence of defects and promote the formation of optimal microstructures (which can be related to the local thermal gradients, solidification velocities, and cooling rates predicted by the models).

The models and understanding of SLM physics developed in this program will be valuable assets as MIT LL expands its AM production to new metals and more complex parts. Prediction of melt pool characteristics and thermal history will facilitate the processing of alloys and metal matrix composites with yield strength, fatigue strength and ductility superior to those of the AM metals presently used at MIT LL. In parts with complex geometries, including features such as thin walls and overhangs, defects, distortion and residual stresses can be predicted and prevented by tuning process parameters, thereby reducing build failures and expediting part qualification. Furthermore, there is continued interest in leveraging MIT LL's core expertise in sensing, imaging, and data processing to integrate high-resolution temperature measurement with SLM. Because only surface measurements of temperature can be made, models of the process will then be indispensable

in the development of algorithms that can use surface temperatures to predict defects that form below the surface and enable real-time forward control of process parameters.

This page intentionally left blank.

This page intentionally left blank.